




Mott memristors based on field-induced carrier avalanche multiplicationFrancesco Peronaci ¹, Sara Ameli ¹, Shintaro Takayoshi,^{1,2} Alexandra S. Landsman ³ and Takashi Oka^{1,4}¹Max Planck Institute for the Physics of Complex Systems, Dresden 01187, Germany²Department of Physics, Konan University, Kobe 658-8501, Japan³Department of Physics, The Ohio State University, 191 West Woodruff Ave, Columbus, Ohio 43210, USA⁴Institute for Solid State Physics, University of Tokyo, Kashiwa 277-8581, Japan

(Received 16 March 2022; accepted 15 February 2023; published 27 February 2023)

We present a theory of Mott memristors whose working principle is the nonlinear carrier avalanche multiplication in Mott insulators subject to strong electric fields. The internal state of the memristor, which determines its resistance, is encoded in the density of doublon and hole excitations in the Mott insulator. In the current-voltage characteristic, insulating and conducting states are separated by a negative-differential-resistance region, leading to hysteretic behavior. Under oscillating voltage, the response of a voltage-controlled, nonpolar memristive system is obtained, with retarded current and pinched hysteresis loop. As a first step towards neuromorphic applications, we demonstrate self-sustained spiking oscillations in a circuit with a parallel capacitor. Being based on electronic excitations only, this memristor is up to several orders of magnitude faster than previous proposals relying on Joule heating or ionic drift.

DOI: [10.1103/PhysRevB.107.075154](https://doi.org/10.1103/PhysRevB.107.075154)**I. INTRODUCTION**

In strongly correlated materials, many-body electronic interactions cannot be treated as a weak perturbation. A spectacular consequence is the breakdown of standard band theory in Mott insulators, which display a charge gap despite having nominally partially-filled bands. Even more interesting, from both fundamental and applied points of view, are states of matter obtained from a Mott insulator by applied pressure or chemical doping [1,2], photo-doping [3–6], or applied electric field [7,8].

A Mott insulator under a sufficiently large electric field eventually displays a metallic response, a phenomenon known as dielectric breakdown. Although the insulator-to-metal transition may result from Joule heating [9,10], there is growing experimental evidence that also purely electronic transitions can occur [11–21]; see Refs. [22–33] for theoretical investigations. Particularly in narrow-gap Mott insulators [13,16] the dielectric breakdown happens via carrier avalanche multiplication, whereby the kinetic energy of accelerated carriers is converted into excitation energy of additional carriers. While a similar mechanism occurs also in semiconductors [34], a distinctive feature of Mott materials is the nonlinearity of the process. Indeed, nonlinear response to applied fields is a fingerprint of strongly correlated insulators, which often display multivalued I - V characteristic with regions of negative

differential resistance $\mathcal{R} \equiv dV/dI$ (V, I : voltage and current across a two-terminal device) [7,8,35–38].

The resistance of Mott insulators may vary over several orders of magnitude across different branches of the I - V curve. Owing to this resistive switch, Mott materials are promising candidates for replacing conventional semiconducting transistors in the field of information processing. More specifically, in neuromorphic applications [39] they are proposed to fabricate memristors [40–43], electronic devices whose resistance depends on the history of the input signal, which are regarded as the building blocks of bio-inspired novel computing architectures [44–48].

From a formal point of view, a voltage-controlled memristive system is defined by its state-dependent resistance, or memristance $M(x)$ (x : state variable) and by the equation of motion $\dot{x} = f(x, V)$. The instantaneous resistance depends, therefore, on the past voltage. From a more empirical perspective, the fingerprint of a memristor is a pinched hysteresis loop in the I - V plane when the device is subject to a bipolar periodic signal [41,42].

Following semiconducting thin films with intertwined electronic and ionic motion [43], diverse other solid-state platforms are being investigated as physical realizations of memristors; in particular Mott materials, using Joule heating to locally trigger the insulating-to-metal transition [49–54]. The timescale of these devices is set by the physical mechanism for the resistance switch and is of the order of milliseconds for ionic drift [43,55] and of nano- to microseconds for Joule heating [50].

In this paper we present a theory of a memristor made of a narrow-gap Mott insulator, whose state variable is the density of doublon excitations, which are the charge carriers. In stark contrast with previous proposals, the resistance switch in this memristor is based on a purely electronic mechanism:

Published by the American Physical Society under the terms of the Creative Commons Attribution 4.0 International license. Further distribution of this work must maintain attribution to the author(s) and the published article's title, journal citation, and DOI. Open access publication funded by the Max Planck Society.

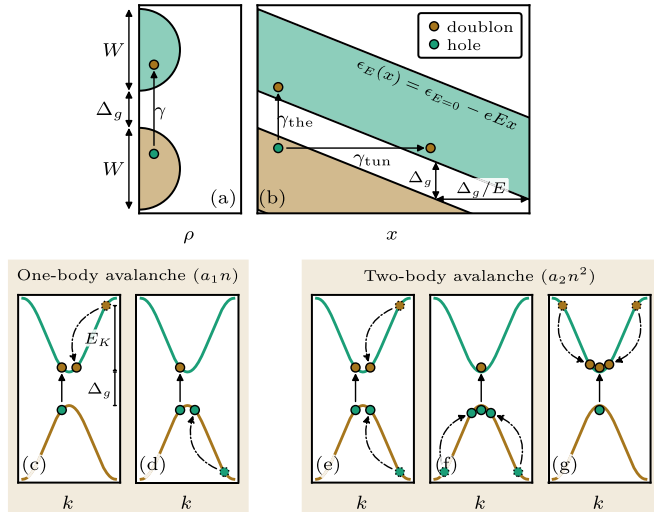


FIG. 1. Hubbard bands and carrier multiplication. (a) Lower and upper Hubbard bands, i. e., one-particle-excitation density of states ρ , with gap Δ_g smaller than bandwidth W ; doublon-hole pair excitation (γ). (b) Band bending in real space x under electric field E and doublon-hole pair creation by thermal activation (γ_{the}) and quantum tunneling (γ_{tun}). [(c)–(g)] Doublon and hole dispersions in momentum space k , with one-body [(c),(d)] and two-body [(e)–(g)] avalanche processes.

the field-induced nonlinear carrier avalanche multiplication. This results, in particular, in a timescale set by the doublon decay time, which is of the order of picoseconds, namely up to several orders of magnitude faster than in previous proposals.

In the following, we illustrate the microscopic working principle in Sec. II, where we present a phenomenological model for the field-induced nonlinear carrier avalanche multiplication. Building on this, in Sec. III we introduce our model of Mott memristor, derive the static current-voltage curve, and study the d.c. transitions between insulating and conducting states. In Sec. IV we study the a.c. response, obtaining the typical behavior of a voltage-controlled, nonpolar memristive system; and derive the steady-state diagram. Finally, in Sec. V, as a first step towards neuromorphic applications, we study a circuit with a parallel capacitor and demonstrate self-sustained current oscillations, reminiscent of the periodic spiking activity of biological neurons.

II. PHENOMENOLOGICAL MODEL OF FIELD-INDUCED CARRIER AVALANCHE MULTIPLICATION IN MOTT INSULATORS

We start by presenting a phenomenological model of Mott insulator as a material with variable concentration of charge carriers. In this model, similarly to electrons and holes in semiconductors, the carriers are doublons and holes, which are one-particle excitations in upper and lower Hubbard bands, respectively, see Fig. 1(a). Note that here we adopt a simplified description and do not consider the dynamical nature of the Mott gap, which is held fixed [56]. Furthermore, we impose the doublon-hole symmetry, such that these excitations differ only for their charge ($\pm e$) and have the

same concentration n , which hereafter is simply referred to as doublon density.

The density of doublon excitations n can be considered as a state variable which determines the conductivity of the material. In this phenomenological model, doublons have charge e , effective mass m^* , and they accelerate in an electric field, before scattering after a typical time τ . This is formalized in the Drude formula for the conductivity,

$$\sigma(n) = e^2(m^*)^{-1}\tau n, \quad (1)$$

which relates the current density j to the electric field E ,

$$j = \sigma(n)E. \quad (2)$$

Similar forms to Eq. (1) also apply to weakly correlated materials, with for example n representing the density of conduction-band electrons. The key difference with the model at hand is in the rate equation for n , in which the strong correlations typical of Mott materials appear as a nonlinear term in the doublon density,

$$\dot{n} = \gamma - n\tau_d^{-1} + (a_1n + a_2n^2)E^2. \quad (3)$$

The source term $\gamma = \gamma_{\text{the}} + \gamma_{\text{tun}}$ describes excitations of doublon-hole pairs induced by thermal fluctuations (γ_{the}) or quantum tunneling across the gap (γ_{tun}), see Fig. 1(b). In principle, these depend on temperature and electric field; here we hold γ fixed and concentrate on the field dependence of the other terms [57]. The second term in Eq. (3) describes the decay of doublon excitations with a typical time τ_d [58]. The equilibrium density, namely the zero-field stationary solution, is $n = \gamma\tau_d \equiv n_0$.

The one-body avalanche term (a_1nE^2), also known as impact ionization, is present in both strongly [28] and weakly correlated materials [34]. It describes a process in which the kinetic energy of a carrier is converted into excitation energy of new carriers via scattering with impurities or phonons [Figs. 1(c) and 1(d)]. The two-body avalanche term ($a_2n^2E^2$), on the other hand, describes many-body scatterings of two excitations kicking out new carriers [Figs. 1(e)–1(g)] and is therefore proportional to the squared carrier density. Since the excitation energy of doublon-hole pairs, Mott gap Δ_g , is provided by the kinetic energy $E_K \leq W$ of accelerated carriers (W : width of Hubbard bands, see Fig. 1), the conditions for one- and two-body avalanche are $\Delta_g \leq W$ and $\Delta_g \leq 2W$ (each carrier has maximum energy $E_K = W$). We refer to a Mott material satisfying these conditions as narrow-gap Mott insulator.

In this paper we mostly consider homogeneous carrier density. In the inhomogeneous case, additional terms proportional to the carrier-density and current-density gradients appear in Eqs. (2), (3), and doublons and holes have to be treated separately, see Appendix C.

In nonzero electric field, Eq. (3) yields two stationary doublon densities, that is the solutions of $\dot{n} = 0$,

$$\bar{n}(E) = \frac{n_0[E_0^2 - AE^2 \pm \sqrt{(E_0^2 - AE^2)^2 - 4E^2E_0^2}]}{2E^2}. \quad (4)$$

Here $E_0 \equiv (\tau_d\sqrt{a_2\gamma})^{-1}$ and $A \equiv a_1(a_2\gamma\tau_d)^{-1}$ is the ratio of the one- to the two-body avalanche term for $n = n_0$. Imposing the solutions (4) to be real and positive yields the condition

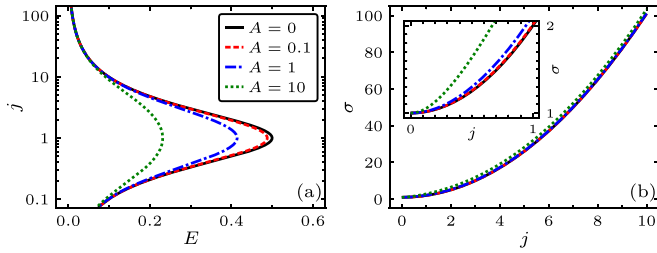


FIG. 2. Stationary conductivity. (a) Stationary current density vs electric field for varying ratio of one- to two-body avalanche. (b) Stationary conductivity vs current density. $j_0 = E_0 = \sigma_0 = 1$.

$E < E_{\text{th}}$, with the threshold electric field

$$E_{\text{th}} = E_0 \frac{\sqrt{1+A} - 1}{A} \approx \frac{E_0}{2} (1 - 0.25A), \quad (5)$$

where the approximation is valid for small A , namely for predominant two-body avalanche. At this threshold, the two branches of Eq. (4) merge, the doublon density is

$$\bar{n}(E_{\text{th}}) = n_0 \frac{A}{\sqrt{1+A} - 1} \approx 2n_0(1 + 0.25A), \quad (6)$$

and the current density reads

$$\bar{j}(E_{\text{th}}) = \sigma(\bar{n}(E_{\text{th}}))E_{\text{th}} = \sigma_0 E_0 \equiv j_0, \quad \sigma_0 \equiv \sigma(n_0). \quad (7)$$

In contrast with the threshold electric field and doublon density, the threshold current density does not depend on the one-body constant a_1 , but only on the two-body constant a_2 (through E_0) and it diverges for $a_2 \rightarrow 0$.

Since the conductivity increases with doublon density, we can interpret the lower branch of Eq. (4) as the slightly perturbed equilibrium insulating state, and the upper branch as a conducting state. The corresponding current density $\bar{j} = \sigma(\bar{n})E$ is plotted in Fig. 2(a). It should be stressed that the two branches correspond to the same microscopic state and differ only in the doublon density; in particular, this theory does not cover the field-induced collapse of the Mott gap. Equation (4) also implies that, within this model, there are no stationary solutions for $E > E_{\text{th}}$, meaning that the material cannot sustain such electric fields. In Fig. 2(b) we plot the stationary conductivity as a function of the current density,

$$\begin{aligned} \bar{\sigma}(j) &= j[\bar{E}(j)]^{-1} \\ &= \frac{\sigma_0 [j^2 + j_0^2 + \sqrt{(j^2 + j_0^2)^2 + 4A j^2 j_0^2}]}{2j_0^2} \\ &\approx \sigma_0 [1 + (j/j_0)^2 + A j^2 (j^2 + j_0^2)^{-1}], \end{aligned} \quad (8)$$

where $\bar{E}(j)$ is the inverse function of $\bar{j}(E) = \sigma(\bar{n}(E))E$ and the approximation is valid for small A . Expressions similar to Eq. (8) have been suggested to explain experiments on a class of charge-transfer insulators [7,35].

The results in Fig. 2 are in qualitative agreement with experiments in which a current is passed through a Mott insulator and the electric field (thus the conductivity) is measured, see e. g., Refs. [37,38]. Indeed, up to this point the treatment is suitable to describe situations in which the current, and not the electric field, is the external parameter. To

show this from a formal point of view, we linearize Eq. (3) around the stationary solution (4) at fixed E or at fixed $j = \sigma(\bar{n}(E))E$. In the former case we get $\tau_d \delta \dot{n} = \pm \delta n [1 - A(E/E_0)^2 - 4(E/E_0)^2]^{1/2}$, which shows that only the lower branch is stable. If we instead fix j , we get $\tau_d \delta \dot{n} = -\delta n [1 + A(j/j_0)^2 (n_0/n)^2]$, which is stable for all current densities. Only in the latter case states with large conductivity are stable and can therefore be observed.

Among the parameters introduced in this section, most relevant are τ_d , E_0 , j_0 , which set the characteristic scales of, respectively, time, electric field, current density. The doublon decay time is typically $\tau_d \sim 1-10$ ps, as measured in ultrafast pump-probe optical spectroscopy [3-6], while electric fields of the order $E_0 \sim 1-10$ kVcm $^{-1}$ and current densities $j_0 \sim 1-10$ mA/cm 2 have been measured in Refs. [7,37,38]. Together with the physical dimensions of the memristor, E_0 and j_0 also set the characteristic scales of, respectively, voltage and current.

III. CURRENT-VOLTAGE CHARACTERISTIC AND INSULATING-CONDUCTING TRANSITIONS

We introduce now our model of Mott memristor as a device composed of a Mott insulator connected in series with a conventional resistor. Adopting the description in Sec. II, the resistance of the Mott insulator is a function of carrier density through the conductivity $\sigma(n)$ [Eq. (1)],

$$R(n) = LS^{-1}[\sigma(n)]^{-1}, \quad (9)$$

where L and S are length and section area. Instead, the conventional resistor has a fixed resistance R_s . The total resistance of the memristor, or memristance, is therefore

$$M(n) = R(n) + R_s, \quad (10)$$

and the doublon density n is its state variable. Attaching a voltage generator V to the memristor, the electric field internal to the Mott material is

$$E = \frac{VR(n)}{L[R(n) + R_s]} = \frac{Vn_0}{L(n_0 + r_s n)}, \quad (11)$$

with $r_s = R_s/R_0$, $R_0 \equiv R(n_0)$. Thus, the electric field does not depend solely on the applied voltage, but also on the doublon density. For small density the resistance of the Mott material is large, $R(n) \gg R_s$, and the field is approximately proportional to the voltage. On the other hand, for large density the resistance of the Mott material drops, $R(n) \ll R_s$, and so does the field. This mechanism is crucial for the stabilization of the conducting state of the memristor, as we discuss in this section.

The state-dependent resistance [Eq. (10)] and the rate equation for the state variable [Eqs. (3) and (11)] define a nonpolar voltage-controlled memristive system [41]. In practice, the fixed term in the resistance corresponds to either the contact resistance, often present especially in two-probe measurements (see e. g., Ref. [36]), or a resistor added to obtain a stable conducting state [7,37,38].

A. Stationary doublon density

The stationary condition is obtained plugging Eq. (11) into Eq. (3) and imposing $\dot{n} = 0$ (we set $A = 0$ hereafter). We solve

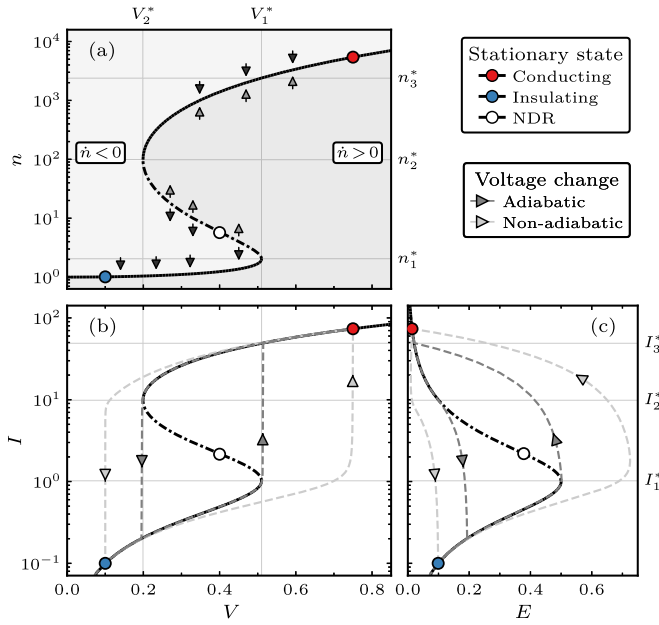


FIG. 3. Stationary I - V characteristic. (a) Doublon density \bar{n} versus voltage. The arrows point up (down) where $\dot{\bar{n}}$ is positive (negative) showing that the solution is unstable if $d\bar{n}/dV < 0$. (b) “S”-shaped I - V curve (solid) and trajectories upon adiabatic and nonadiabatic sweep across $[V_2^*, V_1^*]$ (dashed). (c) Stationary current versus internal field (solid) and same trajectories as in (b) visualized on the I - E plane (dashed). $r_s = 0.01$; $n_0 = V_0 = I_0 = E_0 = 1$.

the resulting equation for V ,

$$\bar{V}(n) = \frac{V_0(n_0 + r_s n)\sqrt{n - n_0}}{n\sqrt{n_0}}, \quad (12)$$

where $V_0 \equiv LE_0$. This is plotted in Fig. 3(a) as n versus $\bar{V}(n)$, which allows us to visualize the stationary density \bar{n} as a function of voltage. This solution is stable only if $d\bar{n}/dV > 0$, namely for \bar{n} outside a range $[n_1^*, n_2^*]$, where these values are therefore obtained imposing

$$\frac{d\bar{V}}{dn} = \frac{V_0(r_s n^2 - n_0 n + 2n_0^2)}{2n^2\sqrt{n_0(n - n_0)}} = 0, \quad (13)$$

which yields

$$n_{1,2}^* = \frac{n_0(1 \pm \sqrt{1 - 8r_s})}{2r_s}. \quad (14)$$

For small r_s we can approximate $n_1^* \approx 2n_0(1 + 2r_s)$ and $n_2^* \approx n_0 r_s^{-1}$. Therefore, the two stable branches are well separated ($n_2^*/n_1^* \approx 0.5r_s^{-1}$) and we can interpret them as the insulating ($n < n_1^*$) and conducting ($n > n_2^*$) states of the memristor. Increasing r_s , the two branches approach each other as $n_2^* - n_1^* = n_0\sqrt{1 - 8r_s}/r_s$ and eventually merge for $r_s = 0.125$. Beyond this value, we have one continuous stable state with no clear separation between insulating and conducting states. In the opposite limit, $r_s \rightarrow 0$, the stable conducting branch vanishes ($n_2^* \rightarrow \infty$). In the remainder of this paper we set $r_s = 0.01$. Between $V_2^* = \bar{V}(n_2^*) \approx 2V_0\sqrt{r_s}$ and $V_1^* = \bar{V}(n_1^*) \approx 0.5V_0(1 + 2r_s)$ insulating and conducting states coexist. In particular, at V_1^* the density is n_1^* on the insulating branch and n_2^* on the conducting branch.

B. Current-voltage characteristic

In the stationary state with voltage $\bar{V}(n)$ and doublon density n , the current through the memristor is

$$\bar{I}(n) = \frac{\bar{V}(n)}{R(n) + R_s} = \frac{I_0\sqrt{n - n_0}}{\sqrt{n_0}}, \quad (15)$$

where $I_0 \equiv V_0 R_0^{-1}$. Plotting Eq. (15) versus Eq. (12) we obtain the current-voltage curve in Fig. 3(b). This has a distinct “S” shape composed of three branches with alternating differential resistance $\mathcal{R} \equiv dV/dI$, which is positive in the stable insulating and conducting branches; and negative in the unstable region in between [negative-differential-resistance region (NDR)].

A voltage sweep across the range $[V_2^*, V_1^*]$ results in a current hysteresis, see Fig. 3(b). If the voltage change is adiabatic, meaning so slow that at each moment the memristor is stationary, then from the insulating branch the current follows the I - V curve up to V_1^* , where a jump discontinuity leads from $I_1^* = \bar{I}(n_1^*) \approx I_0(1 + 2r_s)$ to the conducting branch in $I_3^* = \bar{I}(n_3^*)$. Then, upon decreasing the voltage, the current remains large down to V_2^* where a second discontinuity leads from $I_2^* = \bar{I}(n_2^*) \approx I_0/\sqrt{r_s}$ back to the insulating branch. If the voltage change is nonadiabatic, namely, rapidly increasing and decreasing, the current does not follow thoroughly the I - V curve but instead traces a larger hysteresis area.

In Fig. 3(c) we plot the same quantities as in Fig. 3(b) versus the electric field internal to the Mott insulator. Since current and current density are proportional, $I = jS$, the stationary curve is a rescaled copy of Fig. 2(a) with the crucial difference that this is now stable also for $I > I_2^*$. The trajectories appear different in the I - E plane with respect to the I - V curves; since during the constant-voltage insulating-conducting transitions both current and internal field vary. Also in this case, a nonadiabatic voltage results in a wider trajectory.

Note that in order to plot the stationary curves in Fig. 3 and analytically derive the thresholds $V_{1,2}^*$, we have used the mathematical stratagem to consider n independent variable in Eqs. (12) and (15). If one instead consider V independent, as done in the numerical simulations, the solution of $\dot{n} = 0$ is not as transparent.

C. Delay time and relaxation time

To study the timescales associated with the transitions between insulating and conducting states, we consider a voltage $V(t) = V_i + (V_f - V_i)f(t)$ with a ramp function $f(t) = [1 + \tanh(t - 10)]/2$ and we numerically integrate Eqs. (3) and (11). From the insulating state, as the voltage increases above V_1^* , the transition takes place in two steps [Figs. 4(a) and 4(b)]: first, during a delay time t_D the current remains low; then, it rapidly increases above I_2^* , meaning that the memristor has become conducting. Notice that after the transition $I \propto V_f$ since in the conducting state the memristance is approximately constant $M(n) \approx R_s$.

The delay time is plotted in Fig. 4(c) versus the voltage and for varying initial conditions. While the insulating-to-conducting transition naturally starts from the insulating branch $[n_0, n_1^*]$, here we consider also initial conditions in the

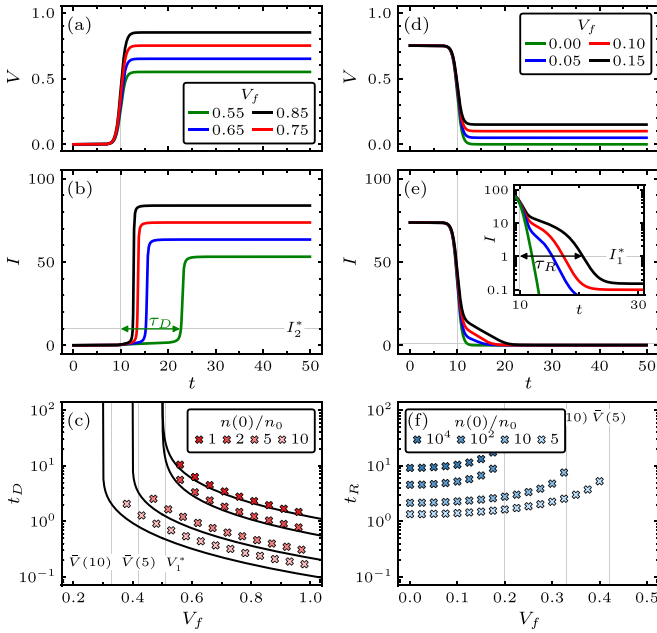


FIG. 4. Delay and relaxation time. (a) Voltage ramp from $V_i = 0$ to $V_f > V_1^*$ and (b) corresponding current evolution. The delay time t_D is the interval between the voltage ramp and when $I = I_2^*$ (see arrow for $V_f = 0.55$). (c) t_D vs V_f for various initial conditions $n(0)$ (markers) and approximation Eq. (17) (solid). (d) Voltage ramp from $V_i = 0.75$ to $V_f < V_2^*$ and (e) corresponding current evolution. The relaxation time t_R is the interval between the voltage ramp and when $I = I_1^*$ (see arrow for $V_f = 0.15$ in the log-scale inset). (f) t_R vs V_f for various initial conditions $n(0)$. Voltage, current, time are in units of $V_0 = 1$ V (e. g., $E_0 = 1$ kVcm $^{-1}$, $L = 10$ μ m), $I_0 = 1$ μ A (e. g., $j_0 = 10$ mA/cm 2 , $S = 100 \times 100$ μ m 2), $\tau_d = 10$ ps. $r_s = 0.01$.

unstable region $[n_1^*, n_2^*]$, which are relevant in the case the voltage changes while the memristor is not at equilibrium. The delay time decreases with increasing voltage and larger initial density. It diverges in V_1^* if the initial density is below $n_1^* \approx 2.02n_0$, or in $\bar{V}(n(0))$ otherwise. This difference can be explained with the aid of the stationary curve in Fig. 3(a), which shows that for $n > n_1^*$ the lower-bound voltage leading to the conducting branch is indeed $\bar{V}(n)$.

To get analytical insight into the delay time and its dependence on voltage and initial density, we solve Eq. (3) in the approximation $E \approx VL^{-1}$ obtaining for $V > V_1^* \approx 0.5V_0$ (see Appendix A):

$$n(t) = \bar{n}_{av} [1 - \Delta \cot [\Delta(t - t_D)/(2\tau_d)]], \quad (16)$$

where $\bar{n}_{av} = 2n_0(V_1^*/V)^2$ and $\Delta = [(V/V_1^*)^2 - 1]^{1/2}$. In this approximation the transition to the conducting state happens where Eq. (16) diverges, giving the delay time

$$t_D = (2\tau_d/\Delta) \cot^{-1} [(n(0) - \bar{n}_{av})/(\bar{n}_{av}\Delta)], \quad (17)$$

which we plot in Fig. 4(c) alongside the numerical result. In the limit $V \rightarrow (V_1^*)^+$ we have $\bar{n}_{av} \rightarrow 2n_0 \approx n_1^*$ and $\Delta \rightarrow 0$. The behavior of t_D depends on whether $n(0)$ is smaller or larger than n_1^* , in the former case it diverges as $t_D \approx 2\tau_d\pi/\Delta$, while in the latter case it stays finite and diverges at a lower voltage $\bar{V}(n(0))$.

Also the transition from the conducting state, as the voltage decreases below V_2^* , takes place in various steps [Figs. 4(d) and 4(e)]: First, the current rapidly decreases; then, it remains high during a relaxation time t_R ; finally, it decreases below I_1^* . The relaxation time is plotted in Fig. 4(f) versus the voltage and for varying initial conditions. Analogously to what discussed for the delay time, we consider initial conditions in the conducting branch $[n_1, \infty]$ as well as in the unstable region $[n_1^*, n_2^*]$. The relaxation time increases with increasing voltage and larger initial density; and diverges in V_2^* if the initial density is above $n_2^* \approx 100n_0$, or in $\bar{V}(n(0))$ otherwise.

The results in this section, in particular the current-voltage characteristic and the delay time, qualitatively agree with various experiments on similar devices [7,8,35–38]. Moreover, the analysis of delay and relaxation times sets the stage for the discussion of the a.c. response, a fundamental characteristic of a memristive system.

IV. RESPONSE TO ALTERNATING VOLTAGE

We proceed now with the study of the a.c. response of the Mott memristor introduced in Sec. III and defined by its state-dependent resistance and state-variable equation of motion [Eqs. (3), (9)–(11)], including the typical memristive features of current retardation and current-voltage pinched hysteresis loop.

A. Time evolution of doublon density and steady-state current

In Figs. 5(a)–5(d) we plot the time evolution of doublon density [obtained by numerical integration of Eqs. (3) and (11)] for various amplitude and frequency of the voltage $V(t) = V_a \cos(\Omega t)$ and for two different initial conditions. We distinguish four qualitatively different steady states. In Figs. 5(a) and 5(b) the steady state is respectively insulating ($n < n_1^*$) or conducting ($n > n_2^*$) independently of the initial condition. In contrast, in the case of Fig. 5(c) there are two possible steady states depending on the initial condition. Finally, in Fig. 5(d) the steady state goes back and forth the insulating and conducting states.

The corresponding steady-state current is plotted in Fig. 5(e)–5(h) for the insulating initial condition and alongside the voltage. The time axis is rescaled with the period $T = 2\pi/\Omega$ and the current and voltage axes with their maxima, for the purpose of comparing various choices of parameters. The insulating steady state [Figs. 5(e) and 5(g)] shows a clear retardation, namely the current profile is distorted with respect to the sinusoidal voltage. Such a retardation effect is the hallmark of memristive systems (see e. g., Ref. [43]) as it exemplifies the inertial change of instantaneous resistance. The effect almost vanishes in the conducting steady state [Fig. 5(f)] because in this case the memristance is approximately constant $M(n) \approx R_s$. Finally, in the steady state back and forth insulating and conducting [Fig. 5(h)] the retardation is very pronounced; in this case the voltage effectively acts as an adiabatic switch, as we discuss below in more detail.

B. Current-voltage pinched hysteresis loop and charge-flux relation

In Figs. 5(i)–5(l) we plot the steady-state current versus the voltage. This curve traces a pinched hysteresis loop (so called

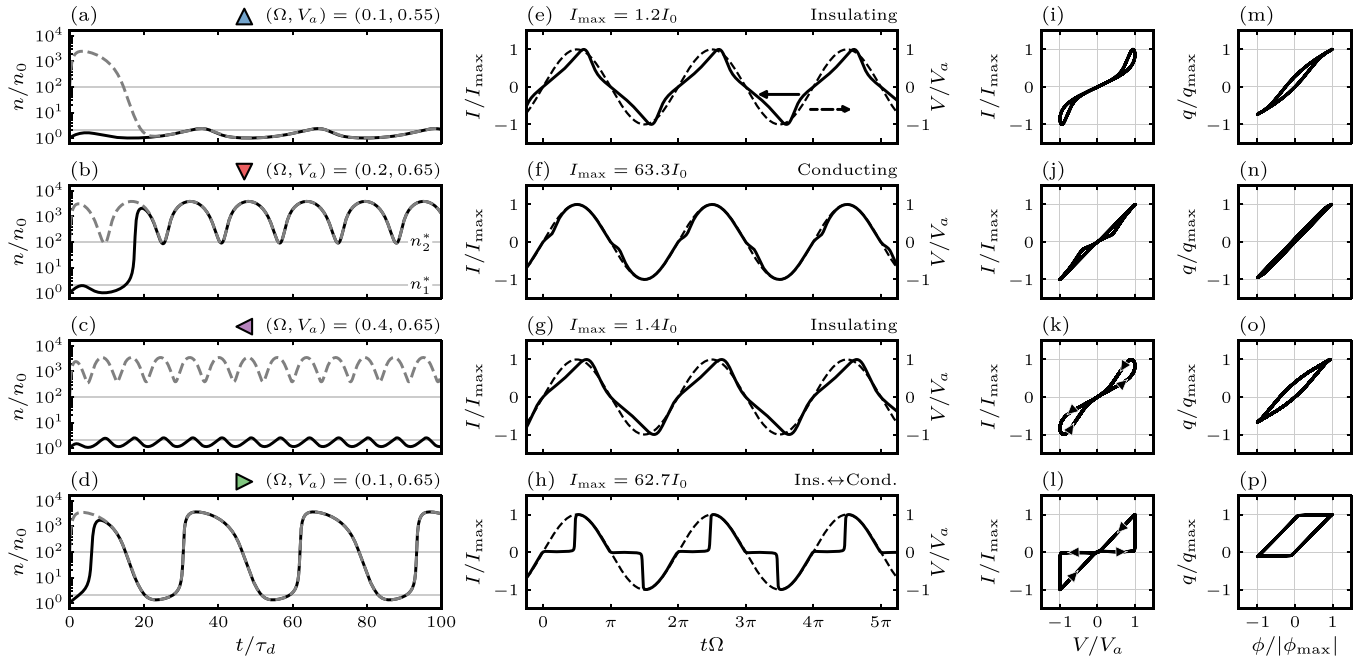


FIG. 5. Memristive behavior in a.c. voltage. (a)-(d) Time evolution of doublon density with initial condition $n(0) = n_0$ (solid) or $n(0) = 100n_0$ (dashed) for various choices of frequency and amplitude (Ω, V_a) (cf. triangle markers in Fig. 6). The state is insulating if $n < n_1^*$ and conducting if $n > n_2^*$. (e)-(h) Corresponding steady-state current (solid) and applied voltage (dashed). (i)-(l) Pinched hysteresis loop in the $I-V$ plane. (m)-(p) Integral of current (charge q) versus integral of voltage (flux ϕ) in the steady state. In (g), (k), (o) only the initial condition $n(0) = n_0$ is considered.

because it crosses the coordinate axes only in the origin), which is considered the empirical definition of a memristive system [41]. Also here, we have rescaled the axes for the sake of comparing the different steady states. The curve slope is the instantaneous inverse differential resistance $\mathcal{R}^{-1} = dI/dV$, meaning that the greater the resistance change, the larger the area encircled by the loop. Indeed, this is more evident in the insulating state [Figs. 5(i) and 5(k)] than in the conducting state [Fig. 5(j)], which has almost constant resistance. In the steady state back and forth insulating and conducting [Fig. 5(l)] the loop is composed of flat, vertical, and steep segments. These correspond to, respectively, insulating state, insulating-to-conducting transition, conducting state, while the conducting-to-insulating transition happens near the origin [cf. arrows in Fig. 5(l)].

The direction of the loop, namely whether it is traced clockwise or anticlockwise, is related to the polarity of the memristive system. In bipolar memristors, e. g., based on ionic drift [43], the resistance changes depending on the sign of the input. Consequently, it is either maximum or minimum in the origin of the $I-V$ plane, and the loop is anticlockwise for positive and clockwise for negative input. In contrast, in the present case the memristor is nonpolar, meaning the resistance change is independent of the sign of the input, cf. Eq. (3). As a result, the loop is anticlockwise both for positive and negative inputs [see arrows in Figs. 5(k) and 5(l)]. Moreover, this implies that the slope in the origin, namely the zero-voltage inverse instantaneous resistance, is the same for increasing or decreasing voltage.

Other characteristics of a memristive system are more conveniently discussed in terms of the relation between charge q

and flux ϕ , namely the integrals of, respectively, current and voltage. Indeed, originally the memristance was introduced as the quantity relating flux to charge [$d\phi = M(q)dq$] similarly to how the resistance relates voltage to current [$dV = R(I)dI$] [40]. The steady-state charge-flux relation is plotted in Figs. 5(m)–5(p). The multivaluedness of this relation is the empirical evidence that the memristive system belongs to the class of nonideal memristors [41]. For ideal memristors, the state-variable equation of motion depends on the input only [$\dot{x} = f(V)$] giving a unique relation between charge and flux [40,43]. Instead, in the broader class of nonideal memristors, the equation of motion depends also on the state variable itself [$\dot{x} = f(x, V)$], which yields a multivalued charge-flux relation, as in this case. On a practical level, an ideal memristor is nonvolatile, meaning its state does not change on zero input [$f(0) = 0$], while the state of a nonideal memristor typically relaxes [$f(x, 0) \neq 0$], which makes it a volatile memory.

C. Steady-state diagram

In Fig. 6 we plot the steady-state diagram as a function of voltage frequency and amplitude. This contains four regions, delimited by the frequency-dependent amplitude thresholds $V_{1,2}^*(\Omega)$, corresponding to each of the steady states discussed above:

- (1) For amplitude smaller than $V_{1,2}^*(\Omega)$ (blue region in Fig. 6) the steady state is insulating, as in Fig. 5(a).
- (2) For amplitude larger than $V_{1,2}^*(\Omega)$ (red region) the steady state is conducting, as in Fig. 5(b).
- (3) For frequency not too low and amplitude within the range $[V_2^*(\Omega), V_1^*(\Omega)]$ (purple region) the steady state is

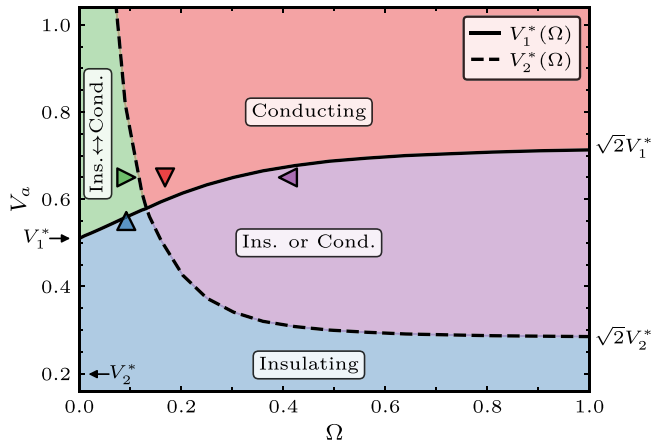


FIG. 6. Steady-state diagram. As a function of frequency and amplitude of a.c. voltage: insulating (blue), conducting (red), going back and forth insulating and conducting (green) and insulating or conducting depending on initial condition (purple). Markers indicate the four choices of parameters in Fig. 5. $V_{1,2}^*(\Omega)$ are the a.c. threshold voltages for insulating-conducting transitions. Axes are in units of $\tau_d^{-1} = 0.1$ THz and $V_0 = 1$ V (e. g., $E_0 = 1$ kVcm $^{-1}$, $L = 10$ μ m).

insulating or conducting depending on the initial condition, as in Fig. 5(c).

(4) For low frequency and amplitude within the range $[V_1^*(\Omega), V_2^*(\Omega)]$ (green region) the steady state goes back and forth insulating and conducting, as in Fig. 5(d).

The a.c. thresholds $V_{1,2}^*(\Omega)$ are closely related to the d.c. thresholds $V_{1,2}^*$ of Sec. III. If we apply a voltage with small amplitude, such that the memristor is insulating, and then gradually increase it, $V_1^*(\Omega)$ is the minimum value at which the memristor becomes conducting. Notice the analogy with V_1^* , which is the minimum voltage to trigger the d.c. insulating-to-conducting transition. However, in the a.c. case two scenarios are possible: the memristor either stays conducting indefinitely, or it goes back to insulating at a later point of the voltage period. The two regions above $V_1^*(\Omega)$ (respectively red and green in Fig. 6) correspond to these two cases. Analogously, applying a voltage with large amplitude, such that the memristor is conducting, and then gradually decreasing it, $V_2^*(\Omega)$ is the amplitude at which the memristor becomes insulating.

To discuss the frequency dependence of $V_{1,2}^*(\Omega)$, it is convenient to separately consider the regimes of low, intermediate, and high frequency.

1. Low frequency

At low frequency, the a.c. response to a voltage $V(t) = V_a \cos(\Omega t)$ is in a sense singular. On the one hand, at zero frequency the voltage reduces to constant. On the other hand, at nonzero albeit low frequency, it successively assumes all values in $[-V_a, V_a]$. In other words, in the low-frequency limit the a.c. voltage is equivalent to an adiabatic sweep, such as considered in Sec. III. Thus, the steady state is insulating if $V_a < V_1^*$ and back and forth insulating and conducting if $V_a > V_1^*$, as for repeated sweeps, cf. Fig. 3(b). Note the absence of conducting steady states in this limit, since no matter how large the amplitude, the memristor invariably turns insulating

during the long interval in which the voltage assumes low values. This is reflected in the divergence of $V_2^*(\Omega)$, while $V_1^*(\Omega)$ is continuous and tends to the d. c. threshold V_1^* .

2. Intermediate frequency

The intermediate-frequency regime can be understood in terms of a competition of timescales: the half-period $\tau_\Omega = \pi/\Omega$; and the delay (τ_D) and relaxation (τ_R) times, namely the timescales for, respectively, the insulating-to-conducting and the conducting-to-insulating transitions. While these were precisely defined in Sec. III for the d.c. transitions, here the discussion is more qualitative and depends only on $\tau_{D,R}$ being, respectively, decreasing and increasing as a function of voltage amplitude.

Since within the range $[V_1^*(\Omega), V_2^*(\Omega)]$ (green region in Fig. 6) there are one insulating-to-conducting and one conducting-to-insulating transition during each half a period [cf. Figs. 5(d) and 5(h)], this region is characterized by the relation $\tau_D, \tau_R < \tau_\Omega$. Indeed, if either timescale were longer than τ_Ω , the corresponding transition could not take place. This suggests the interpretation of $V_{1,2}^*(\Omega)$ as the curves where, respectively, $\tau_\Omega = t_D$ and $\tau_\Omega = t_R$. Crossing for example $V_1^*(\Omega)$, the region with insulating steady states is characterized by $t_R < \tau_\Omega < t_D$, that is by the inhibition of the insulating-to-conducting transition. Within this perspective, $V_1^*(\Omega)$ increases with frequency because—as τ_Ω decreases—a larger voltage amplitude is needed to match the condition $\tau_\Omega = t_D$.

Where $V_{1,2}^*(\Omega)$ intersect each other, the timescales are all equal: $\tau_\Omega = t_D = t_R$. Crossing this point at constant voltage amplitude, τ_Ω becomes at the same time shorter than both $\tau_{D,R}$, meaning that both the insulating-to-conducting and the conducting-to-insulating transitions are inhibited, and the memristor remains in the same state as the initial condition (purple region in Fig. 6).

3. High frequency

The behavior at high frequency is better illustrated in terms of the infinite-frequency limit, in which the voltage is equivalent to a d.c. $V_a/\sqrt{2}$. Indeed, the voltage enters the equation of motion [Eqs. (3) and (11)] through the square $[V_a \cos(\Omega t)]^2$, which at high frequency is equivalent to its average $V_a^2/2$. The steady state is therefore insulating if $V_a < \sqrt{2}V_1^*$ and conducting if $V_a > \sqrt{2}V_2^*$. Similarly to the d.c. coexistence region, in the range $[\sqrt{2}V_2^*, \sqrt{2}V_1^*]$ the steady state is insulating or conducting depending on the initial condition. Note that in the high-frequency limit $V_{1,2}^*(\Omega)$ tend to constant. To reconcile this with the previous discussion in terms of timescales, we have to consider that at high frequency the transitions can happen across multiple voltage periods.

V. SELF-SUSTAINED OSCILLATIONS AND SPIKING BEHAVIOR

We study now a first use case of the Mott memristor in electric circuits. In the circuit in Fig. 7(a) the memristor is connected in parallel with a capacitor C and is attached to a voltage generator V_ℓ through a load resistor R_ℓ . This setup allows us to study self-sustained current oscillations as

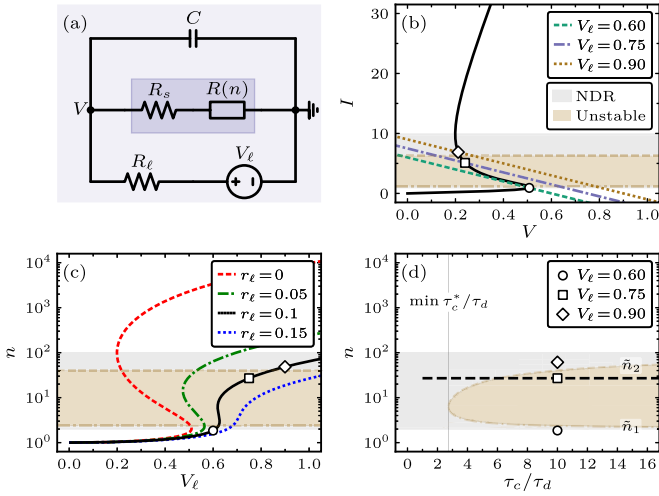


FIG. 7. Spiking circuit and its properties. (a) Circuit with load voltage V_ℓ , load resistor R_ℓ and capacitor C in parallel with the memristor $[R_s + R(n)]$. (b) Fixed points at the intersection of memristor I - V curve (black) with load lines $I = (V_\ell - V)R_\ell^{-1}$. (c) Fixed-point doublon density vs load voltage. (d) Boundaries $\tilde{n}_{1,2}$ of the region with limit cycles (brown) as a function of fixed-point doublon density and τ_c/τ_d ; and NDR region (gray). The same regions are highlighted in (b) and (c) for $\tau_c/\tau_d = 10$. Markers in (b)–(d) correspond to fixed points in Fig. 8; the dashed line in (d) to fixed points in Fig. 9. $n_0 = V_0 = I_0 = 1$.

observed, e. g., in Refs. [36–38]; a phenomenon at the basis of spiking-based computational schemes.

A. Nullclines and fixed point

The equation for the voltage V across the memristor is obtained applying Kirchhoff's law of current conservation at the nodes of the circuit in Fig. 7(a),

$$C\dot{V} + V(R_s + R(n))^{-1} + (V - V_\ell)R_\ell^{-1} = 0, \quad (18)$$

which are the currents through, respectively, capacitor, memristor, and voltage generator. Equation (18) has to be solved together with the rate equation for the doublon density [Eqs. (3) and (11)]. Defining $r_\ell = R_\ell/R_0$, $r_t = r_s + r_\ell$ and the timescale $\tau_c = R_\ell C$ we rewrite these equations as a dynamical system

$$\tau_c \dot{V} = V_\ell - V(r_t n + n_0)(r_s n + n_0)^{-1}, \quad (19a)$$

$$\tau_d \dot{n} = n_0 - n + n_0 n^2 (V/V_0)^2 (r_s n + n_0)^{-2}. \quad (19b)$$

The fixed point of this system is at the intersection of the so-called nullclines, namely the curves along which $\dot{V} = 0$ and $\dot{n} = 0$, which read respectively

$$V = V_\ell (r_s n + n_0)(r_t n + n_0)^{-1}, \quad (20a)$$

$$V = V_0 (r_s n + n_0) \sqrt{n - n_0} (n \sqrt{n_0})^{-1}. \quad (20b)$$

We subtract now the nullclines and, similarly to Sec. III, we solve the resulting equation for V_ℓ , thereby expressing the fixed-point doublon density as the inverse function of

$$\tilde{V}_\ell(n) = \frac{V_0 (r_t n + n_0) \sqrt{n - n_0}}{n \sqrt{n_0}}. \quad (21)$$

This can also be obtained imposing the intersection of the so-called load line $I = (V_\ell - V)R_\ell^{-1}$ with the I - V curve of the Mott memristor [Eqs. (12) and (15)], see Fig. 7(b), since at the fixed point the same current flows through voltage generator and memristor [cf. Eq. (18) with $C\dot{V} = 0$].

Because the current through the capacitor is zero at the fixed point, the resistances R_s and R_ℓ are in series and the circuit reduces to the situation considered in Sec. III with the substitutions $V \rightarrow V_\ell$ and $R_s \rightarrow R_s + R_\ell$, which indeed make Eq. (21) identical to Eq. (12). Therefore, the same analysis applies here: if $r_t > 0.125$ the solution is unique, while if $r_t < 0.125$ there is a region with three solutions, see Fig. 7(c). Together with $r_s = 0.01$, we set hereafter $r_\ell = 0.1$, which gives $r_t = 0.11$.

Depending on load voltage and load resistor, the fixed point can be in the NDR region of the Mott memristor, see Figs. 7(b)–7(d), which is necessary for having limit-cycle self-sustained oscillations, as we discuss in the following.

B. Limit-cycle oscillations

Self-sustained oscillations are periodic solutions of a dynamical system, such as Eqs. (19), in absence of any periodic input. In the system configuration space (here the n - V plane) the corresponding trajectories are limit cycles, namely isolated closed trajectories, which either attract or repel nearby ones [59]. Simply stated, the conditions for a limit cycle are the nonlinearity of the system and the instability of its fixed point. In this case, the former is provided by the nonlinear rate equation for the doublon density. The latter is satisfied if the fixed-point doublon density is between the values (see Appendix B)

$$\tilde{n}_{1,2} = \frac{n_0 [\tau_c - \tau_d \pm \sqrt{(\tau_c - \tau_d)^2 - 8\tau_c(r_s \tau_c + r_t \tau_d)}]}{r_s \tau_c + r_t \tau_d}. \quad (22)$$

Once the load voltage—thus the fixed-point doublon density—is chosen, Eq. (22) gives an implicit expression for the critical τ_c^* , which varies with the fixed-point doublon density and whose minimum is obtained setting to zero the argument of the square root in Eq. (22),

$$\min \tau_c^* = \frac{\tau_d [(1 + 4r_\ell) + \sqrt{(1 + 4r_\ell)^2 - (1 - 8r_s)}]}{1 - 8r_s}. \quad (23)$$

The region $[\tilde{n}_1, \tilde{n}_2]$ is included in the NDR region of the memristor, coinciding with it in the limit of large τ_c . As depicted in Fig. 7(d), to enter this region one can either tune the load voltage (thus the doublon density) or the capacitor (thus the characteristic time τ_c). At this point, a supercritical Hopf bifurcation takes place [59], namely the fixed point loses stability and a limit cycle arises.

1. Tuning the load voltage

At fixed τ_c we consider three load voltages such that the fixed-point doublon density is below, inside, or above the unstable region $[\tilde{n}_1, \tilde{n}_2]$, see Figs. 7(b)–7(d). For each load voltage we numerically integrate Eqs. (19) with varying initial conditions and plot the trajectories in the n - V plane in Figs. 8(a)–8(c). Outside the unstable region ($V_\ell = 0.60, 0.90$) all trajectories tend to the fixed point. Notice that this

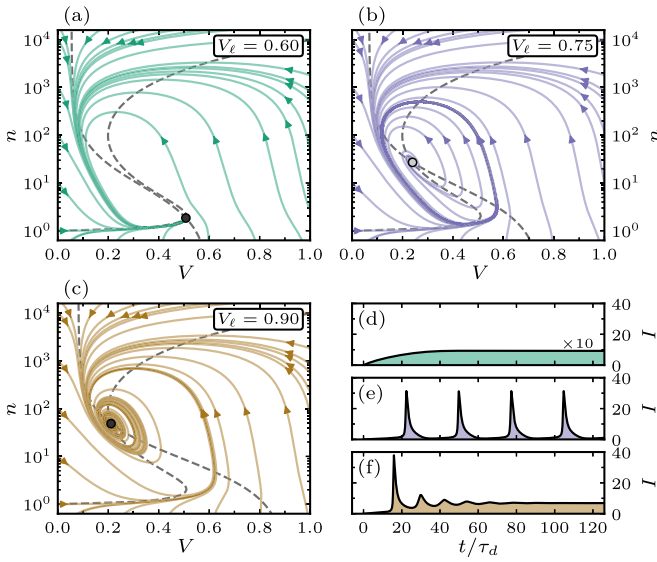


FIG. 8. Bifurcation tuning the load voltage. [(a)–(c)] Trajectories (solid) and nullclines (dashed) in n - V plane for three load voltages and $\tau_c = 10$ [see markers in Figs. 7(b)–7(d)]. The trajectories converge to the fixed point in (a) and (c); or to a limit cycle around the fixed point in (b). [(d)–(f)] Current profile for the same parameters and initial condition $(n_0, 0)$ with spiking behavior corresponding to the limit cycle (e). $r_\ell = 0.1$; $n_0 = V_0 = I_0 = 1$.

implies the absence of closed trajectories. In stark contrast, inside the unstable region ($V_\ell = 0.75$) there is an isolated closed trajectory (i. e., a limit cycle), which attracts all other trajectories. Notice that the limit cycle is around the unstable fixed point. In this case there is no stationary stable solution and, despite the constant load voltage, density and voltage oscillate indefinitely. In other words, the system undergoes limit-cycle self-sustained (or autonomous) oscillations.

The current profile is markedly different in the three cases. Let us consider [see Figs. 8(d)–8(f)] the trajectories with initial condition $(n_0, 0)$. For $V_\ell = 0.60$ the current increases monotonically to the stable fixed point, which is on the insulating branch, see Fig. 8(d). In contrast, for $V_\ell = 0.90$ the stable fixed point is near the conducting branch and is reached only after a transient, which in the n - V plane takes the form of a spiral around the fixed point [Fig. 8(c)], and the current profile has a single spike followed by damped oscillations, see Fig. 8(f).

Finally, corresponding to the limit cycle, for $V_\ell = 0.75$ the current has periodic spiking, see Fig. 8(e). Each spike consists of a sudden increase and a similarly rapid, but slower, decrease. These are due to repeated transitions between the memristor insulating and conducting states, Note that this is consistent with the spiking behavior of biological neurons, in which the neural-cell membrane also transitions between insulating and conducting in the course of an oscillation [60].

2. Tuning the capacitor

In Fig. 9 we plot the trajectories obtained by numerical solution of Eqs. (19) with initial condition $(n_0, 0)$, fixed load voltage and varying τ_c . With its location unaltered, the fixed point loses stability across a critical $\tau_c^* \approx 6.06 \tau_d$ (for $V_\ell =$

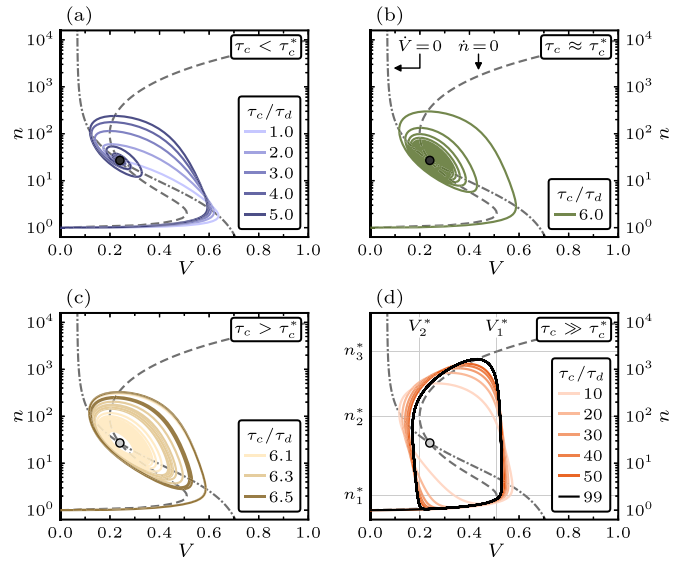


FIG. 9. Bifurcation tuning the capacitor. Trajectories (solid) and nullclines (dashed) in n - V plane for $V_\ell = 0.75$ and varying τ_c [see dashed line in Fig. 7(d)] with initial condition $(n_0, 0)$. The fixed point is stable in (a) and (b); and unstable in (c) and (d) where it is encircled by a limit cycle whose area and size change with τ_c . For very large τ_c (d) the limit cycle tend to an adiabatic hysteresis loop [cf. Figs. 3(a) and 3(b)]. $r_\ell = 0.1$; $n_0 = V_0 = 1$.

0.75), see Fig. 7(d). It is stable for $\tau_c < \tau_c^*$ and reached after a number of oscillations, which become more dense as τ_c^* is approached. As soon as $\tau_c > \tau_c^*$, the fixed point becomes unstable and a small limit cycle appears. Increasing τ_c further, the limit cycle grows and tends to a loop with segments at constant voltage connecting lower and upper branches of the $\dot{n} = 0$ nullcline, see Fig. 9(d). Since this nullcline is nothing but the stationary doublon density \bar{n} versus the voltage [cf. Fig. 3(a)] this limit cycle is equivalent to the hysteresis loop in adiabatic voltage considered in Sec. III. In other words, in this limit the circuit behaves like a relaxation oscillator [59].

The limit-cycle current spikes can be characterized by height (difference between maximum and minimum) and period, see Fig. 10. Evidently, these quantities are only defined for $\tau_c \geq \tau_c^*$. At τ_c^* we have the typical behavior for a supercritical Hopf bifurcation [59]: the height grows from zero (the limit cycle has vanishing amplitude) while the period is finite

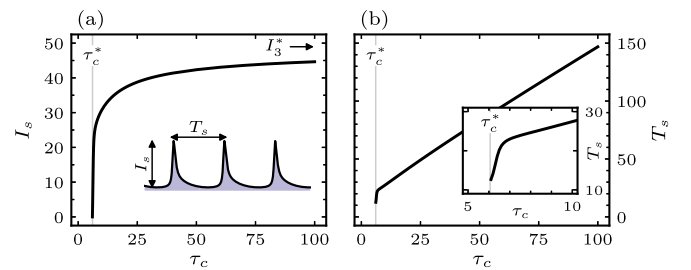


FIG. 10. Characterization of periodic spiking. (a) Height and (b) period of current spikes along the limit cycle [see inset in (a)] as a function of τ_c at fixed $V_\ell = 0.75$ and $r_\ell = 0.1$. Current, time are in units of $I_0 = 1 \mu\text{A}$ (e. g., $j_0 = 10 \text{ mA/cm}^2$, $S = 100 \times 100 \mu\text{m}^2$, $\tau_d = 10 \text{ ps}$).

and equal to $2\pi[\det(J)]^{-1/2} \approx 12\tau_d$, with J the Jacobian of the dynamical system (19) at the fixed point (see Appendix B). Increasing τ_c , the height first rapidly increases, then it slowly saturates to a value close to I_3^* , which is, together with I_1^* , the stationary current at the threshold voltage V_1^* , cf. Fig. 3(b). At the same time, already at $\tau_c \approx 7\tau_d$, the period is linear in τ_c , showing a decoupling of timescales for doublon density and voltage, as expected for a relaxation oscillator.

VI. CONCLUSIONS

We have proposed the narrow-gap Mott insulator as a compact realization of a type of memristor based on the field-induced carrier avalanche multiplication. Due to this purely electronic mechanism for the resistive switch, this Mott memristor has a characteristic timescale set by the doublon-excitation decay time $\tau_d \sim 1\text{--}10$ ps, which is up to several orders of magnitude faster than in devices based on Joule heating or ionic drift.

As a first step we have put forward a phenomenological description of the field-induced carrier avalanche in Mott insulators, in which the conductivity depends on the carrier density, whose rate equation contains the nonlinear scattering terms induced by strong correlations. The model describes a resistive switch due to a large increase in carrier concentration, which we regard as most important in certain Mott materials, for instance organic one-dimensional charge-transfer crystals [7,35] and one-dimensional cuprates Sr_2CuO_3 and SrCuO_2 [8], whose experimental curves have a good qualitative agreement with our results. Effects such as gap suppression and filament formation have not a major role in this description and for simplicity are not included in the theory. For instance, experiments on the Mott insulator Ca_2RuO_4 have ruled out, for these specific material and experimental conditions, gap closing [14,15] and filament formation [21].

Building on the phenomenological model, we have introduced the Mott memristor as a device made of a Mott material in series with a conventional resistor; and we have derived its current-voltage curve, as well as the transitions between conducting and insulating states. While the very definition qualifies the model as a nonpolar, voltage-controlled memristive system, we have analyzed in detail its a.c. response, including current retardation, pinched hysteresis loop, steady-state diagram. Finally, we have considered a circuit with a capacitor in parallel with the memristor and demonstrated self-sustained current oscillations and periodic spiking behavior, consistent with the periodic activity of biological neurons.

Particularly compelling for the future further characterization of the Mott memristor, are the steady states that we found in a.c. voltage, that alternate between insulating and conducting. There, the carrier avalanche multiplication leads to periodic rapid current increases, which, in appropriate experimental setups, would yield a strong high harmonic generation, whose spectrum would bear the distinct signature of the carrier avalanche multiplication, namely those of an electronic excitation, much faster than other mechanisms such as ionic drift and lattice distortions. Moreover, the resulting synchronization of the high harmonics with the driving voltage would

allow for refined control over the emission process, much alike currently possible in isolated atoms [61,62].

While similar devices have been subject of intensive experimental study [7,8,35–38], here they are proposed as memristors. Moreover, our paper provides a comprehensive theory of the key features of those prior studies: threshold electric field, negative differential resistance (NDR), multi-valued current-voltage characteristic, delay time, and current oscillations. At the same time, our proposal consists of a tractable set of equations; which stands in contrast with previous more complicated models, see e. g., Ref. [50], and results in two valuable features. First, we are able to derive analytical expressions, such as the boundaries of the NDR region and the conditions for limit-cycle oscillations. Second, and perhaps more importantly, it makes promising to include the model into the description of circuits of growing complexity, in the quest for bio-inspired novel computing architectures.

ACKNOWLEDGMENTS

A.S.L. acknowledges funding from the Center for Emergent Materials, an NSF MRSEC, under 241 Grant No. DMR-201187.

APPENDIX A: DERIVATION OF EQS. (16) AND (17)

In this Appendix we derive Eqs. (16) and (17) of Sec. III for doublon density and delay time of the d. c. insulating-to-conducting transition. To simplify the exposition, we set $\tau_d = n_0 = E_0 = 1, A = 0$. Then Eq. (3) is rewritten as

$$\dot{n} = 1 - n + n^2 E^2. \quad (\text{A1})$$

The two stationary solutions are $\bar{n} = \bar{n}_{\text{av}}(1 \pm i\Delta)$ where $\bar{n}_{\text{av}} = 1/(2E^2)$ and $\Delta = \sqrt{4E^2 - 1}$ [cf. Eq. (4)] and are real only if $E < E_{\text{th}} = 0.5$ [cf. Eq. (5)]. Since during the delay time the doublon density does not change much, we approximate the field in the Mott insulator as constant, $E \approx VL$, which is equivalent to approximating $r_s \approx 0$, yielding $V_1^* \approx 0.5V_0$ and $n_1^* \approx 0.5n_0$. Equation (A1) can then be solved with a variable change,

$$n = -\dot{x}/(xE^2), \quad (\text{A2})$$

$$\ddot{x} + \dot{x} + E^2 x = 0. \quad (\text{A3})$$

The general solution of the transformed equation (A3) is $x = \alpha_1 e^{s_1 t} + \alpha_2 e^{s_2 t}$ where $s_{1,2} = (-1 \pm i\Delta)/2$. Substituting this back into (A2) yields the solution of Eq. (A1),

$$n = \bar{n}_{\text{av}} \left(1 - i\Delta \frac{\alpha_1 e^{i\Delta t/2} - \alpha_2 e^{-i\Delta t/2}}{\alpha_1 e^{i\Delta t/2} + \alpha_2 e^{-i\Delta t/2}} \right). \quad (\text{A4})$$

Notice that the solution of (A3) depends on both $\alpha_{1,2}$ while Eq. (A4) depends only on their ratio. To proceed, we parametrize $\alpha_{1,2} = \pm \exp(\mp i\Delta t_D/2)$ and obtain

$$n = \bar{n}_{\text{av}} [1 - \Delta \cot[(\Delta/2)(t - t_D)]], \quad (\text{A5})$$

$$t_D = (2/\Delta) \cot^{-1}[(n(0) - \bar{n}_{\text{av}})/(\Delta \bar{n}_{\text{av}})], \quad (\text{A6})$$

which coincide with Eqs. (16) and (17).

Up to now we have considered the electric field above threshold $E > E_{\text{th}}$, which is equivalent to $V > V_1^*$ and makes

Δ and Eqs. (A5) and (A6) real. In the limit $V \rightarrow V_1^*$ we have $\Delta \rightarrow 0$, $\bar{n}_{\text{av}} \rightarrow 2n_0 \approx n_1^*$ and the behavior of the delay time Eq. (A6) depends on the initial condition,

$$t_D \approx \begin{cases} 2\pi/\Delta, & \text{if } n(0) < n_1^*, \\ 2n_1^*/(n(0) - n_1^*), & \text{if } n(0) > n_1^*. \end{cases} \quad (\text{A7})$$

Indeed with a large initial density the transition happens even below threshold. In this case we have to choose $\alpha_{1,2}$ differently or, alternatively, we can analytically continue Eqs. (A5) and (A6) with $\tilde{\Delta} = i\Delta$, which yields

$$n = \bar{n}_{\text{av}}[1 - \tilde{\Delta} \coth[(\tilde{\Delta}/2)(t - t_D)]], \quad (\text{A8})$$

$$t_D = (2/\tilde{\Delta}) \coth^{-1}[(n(0) - \bar{n}_{\text{av}})/(\tilde{\Delta}\bar{n}_{\text{av}})]. \quad (\text{A9})$$

In this case the delay time diverges for $n(0) = \tilde{\Delta}(n_{\text{av}} + 1)$, namely for $V = \tilde{V}(n(0))$, as shown in Fig. 4(c).

APPENDIX B: DERIVATION OF EQ. (22)

In this Appendix we derive Eq. (22) for the region with limit cycle in Sec. V. A limit cycle is guaranteed to exist by the Poincaré–Bendixson theorem when the system is confined in a region with no stable fixed point therein [59]. Such a trapping region is (with $V_\ell r_t r_s^{-1} > V_1^*$) $\{(n, V) \in [0, \bar{n}(V_\ell r_t r_s^{-1})] \times [0, V_\ell r_t r_s^{-1}]\}$. The fixed point turns from stable to unstable (Hopf bifurcation) when, with positive determinant, the trace of the Jacobian becomes positive. For the system (19) the Jacobian reads

$$J(n, V) = \begin{pmatrix} -\frac{r_t n + n_0}{\tau_c(r_s n + n_0)} & -\frac{V r_t n_0}{\tau_c(r_s n + n_0)^2} \\ \frac{2n^2 n_0 V V_0^{-2}}{\tau_d(r_s n + n_0)^2} & -\frac{1}{\tau_d} + \frac{2n n_0^2 (V/V_0)^2}{\tau_d(r_s n + n_0)^3} \end{pmatrix}. \quad (\text{B1})$$

Plugging Eq. (20b) for the $\dot{n} = 0$ nullcline into Eq. (B1), we obtain the Jacobian as a function of the fixed-point doublon density,

$$J(n) = \begin{pmatrix} -\frac{r_t n + n_0}{\tau_c(r_s n + n_0)} & -\frac{V_0 r_t [n_0(n - n_0)]^{1/2}}{\tau_c n(r_s n + n_0)} \\ \frac{2n[n_0(n - n_0)]^{1/2}}{\tau_d V_0(r_s n + n_0)} & -\frac{-r_s n^2 + n n_0 - 2n_0^2}{\tau_d n(r_s n + n_0)} \end{pmatrix}, \quad (\text{B2})$$

whose determinant and trace read

$$\det(J) = \frac{r_t n^2 - n_0 n + 2n_0^2}{\tau_d \tau_c (r_s n + n_0) n}, \quad (\text{B3})$$

$$\text{tr}(J) = \frac{\tau_c(-r_s n^2 + n_0 n - 2n_0^2) - \tau_d(r_t n^2 + n_0 n)}{\tau_d \tau_c (r_s n + n_0) n}. \quad (\text{B4})$$

The sign of the determinant does not depend on τ_c and is positive for n outside the range $[\hat{n}_1, \hat{n}_2]$ with $\hat{n}_{1,2} = n_0(1 \pm \sqrt{1 - 8r_t})(2r_t)^{-1}$. The sign of the trace depends on τ_c . Notice that a necessary condition for the trace to vanish is $(-r_s n^2 + n_0 n - 2n_0^2) > 0$, which is the same condition for the NDR region of the memristor, cf. Eq. (13), demonstrating that the region with limit-cycle oscillations is a subset of the NDR region, as depicted in Figs. 7(b)–7(d). Imposing the trace to be positive we get the condition that n should be outside the range $[\tilde{n}_1, \tilde{n}_2]$ with $\tilde{n}_{1,2}$ given in Eq. (22).

APPENDIX C: INHOMOGENEOUS CASE

In this Appendix we derive the additional terms to the model of Secs. II and III in order to deal with inhomogeneous carrier and current densities. Here we separately consider holes and doublons, with charge $\pm e$, density n_\pm , current density j_\pm . Moreover, we define $n = (n_+ + n_-)/2$ such that for homogeneous and equal densities $n_+ = n_- = n$ the equations of Secs. II and III are retrieved.

In presence of a carrier-density gradient, the current density acquires a diffusion term (D : diffusion constant),

$$j_\pm = \sigma(n_\pm)E \mp eD\nabla n_\pm. \quad (\text{C1})$$

Note that the sign of charge enters only the second term in Eq. (C1) since the conductivity $\sigma(n_\pm)$ depends on the squared charge [cf. Eq. (1)]. For the continuity condition, the rate equation for the carrier density acquires a term proportional to the current-density gradient,

$$\dot{n}_\pm = \gamma - n_\pm \tau_d^{-1} + (a_1 n + a_2 n^2)E^2 \mp e^{-1} \nabla j_\pm. \quad (\text{C2})$$

Plugging Eq. (C1) into Eq. (C2) yields two additional terms, as compared to Eq. (3): $\mp e^{-1} \nabla[\sigma(n_\pm)E]$ resolves into contributions proportional to carrier-density and field gradients; $D\nabla n_\pm$ is the carrier diffusion. Note that the field-induced carrier-avalanche term $(a_1 n + a_2 n^2)E^2$ is the same for holes and doublons.

The electric field in Eqs. (C1) and (C2) has two terms, $E = E_{\text{ext}} + E_{\text{int}}$. The external field is given, as in Sec. III, by the voltage drop across the Mott material,

$$E_{\text{ext}} = \frac{VR}{L[R + R_s]}, \quad R = \frac{2}{S} \int_0^L \frac{dx}{\sigma(n_+) + \sigma(n_-)} \quad (\text{C3})$$

where the resistance of the material depends on the total carrier density and, for simplicity, we take the carrier density varying only along its length. The internal field is given by Poisson's equation (ϵ : dielectric constant),

$$\nabla E_{\text{int}} = e(n_+ - n_-)\epsilon^{-1}. \quad (\text{C4})$$

Solving Eqs. (C2), (C3), (C4) yields the time evolution of the inhomogeneous hole and doublon densities.

- [1] M. Imada, A. Fujimori, and Y. Tokura, Metal-insulator transitions, *Rev. Mod. Phys.* **70**, 1039 (1998).
 [2] P. A. Lee, N. Nagaosa, and X.-G. Wen, Doping a Mott insulator: Physics of high-temperature superconductivity, *Rev. Mod. Phys.* **78**, 17 (2006).

- [3] S. Iwai, M. Ono, A. Maeda, H. Matsuzaki, H. Kishida, H. Okamoto, and Y. Tokura, Ultrafast Optical Switching to a Metallic State by Photoinduced Mott Transition in a Halogen-Bridged Nickel-Chain Compound, *Phys. Rev. Lett.* **91**, 057401 (2003).

- [4] L. Perfetti, P. A. Loukakos, M. Lisowski, U. Bovensiepen, H. Berger, S. Biermann, P. S. Cornaglia, A. Georges, and M. Wolf, Time Evolution of the Electronic Structure of $1T - \text{TaS}_2$ Through the Insulator-Metal Transition, *Phys. Rev. Lett.* **97**, 067402 (2006).
- [5] H. Okamoto, H. Matsuzaki, T. Wakabayashi, Y. Takahashi, and T. Hasegawa, Photoinduced Metallic State Mediated by Spin-Charge Separation in a One-Dimensional Organic Mott Insulator, *Phys. Rev. Lett.* **98**, 037401 (2007).
- [6] H. Okamoto, T. Miyagoe, K. Kobayashi, H. Uemura, H. Nishioka, H. Matsuzaki, A. Sawa, and Y. Tokura, Ultrafast charge dynamics in photoexcited Nd_2CuO_4 and La_2CuO_4 cuprate compounds investigated by femtosecond absorption spectroscopy, *Phys. Rev. B* **82**, 060513(R) (2010).
- [7] Y. Tokura, H. Okamoto, T. Koda, T. Mitani, and G. Saito, Nonlinear electric transport and switching phenomenon in the mixed-stack charge-transfer crystal tetrathiafulvalene-p-chloranil, *Phys. Rev. B* **38**, 2215(R) (1988).
- [8] Y. Taguchi, T. Matsumoto, and Y. Tokura, Dielectric breakdown of one-dimensional Mott insulators Sr_2CuO_3 and SrCuO_2 , *Phys. Rev. B* **62**, 7015 (2000).
- [9] A. A. Fursina, R. G. S. Sofin, I. V. Shvets, and D. Natelson, Origin of hysteresis in resistive switching in magnetite is Joule heating, *Phys. Rev. B* **79**, 245131 (2009).
- [10] A. Zimmers, L. Aigouy, M. Mortier, A. Sharoni, S. Wang, K. G. West, J. G. Ramirez, and I. K. Schuller, Role of Thermal Heating on the Voltage Induced Insulator-Metal Transition in VO_2 , *Phys. Rev. Lett.* **110**, 056601 (2013).
- [11] L. Cario, C. Vaju, B. Corraze, V. Guiot, and E. Janod, Electric-field-induced resistive switching in a family of Mott insulators: Towards a new class of RRAM memories, *Adv. Mater.* **22**, 5193 (2010).
- [12] M. Liu, H. Y. Hwang, H. Tao, A. C. Strikwerda, K. Fan, G. R. Keiser, A. J. Sternbach, K. G. West, S. Kittiwatanakul, J. Lu *et al.*, Terahertz-field-induced insulator-to-metal transition in vanadium dioxide metamaterial, *Nature (London)* **487**, 345 (2012).
- [13] V. Guiot, L. Cario, E. Janod, B. Corraze, V. T. Phuoc, M. Rozenberg, P. Stoliar, T. Cren, and D. Roditchev, Avalanche breakdown in $\text{GaTa}_4\text{Se}_{8-x}\text{Te}_x$ narrow-gap Mott insulators, *Nat. Commun.* **4**, 1722 (2013).
- [14] F. Nakamura, M. Sakaki, Y. Yamanaka, S. Tamaru, T. Suzuki, and Y. Maeno, Electric-field-induced metal maintained by current of the Mott insulator Ca_2RuO_4 , *Sci. Rep.* **3**, 2536 (2013).
- [15] R. Okazaki, Y. Nishina, Y. Yasui, F. Nakamura, T. Suzuki, and I. Terasaki, Current-induced gap suppression in the Mott insulator Ca_2RuO_4 , *J. Phys. Soc. Jpn.* **82**, 103702 (2013).
- [16] P. Stoliar, L. Cario, E. Janod, B. Corraze, C. Guillot-Deudon, S. Salmon-Bourmand, V. Guiot, J. Tranchant, and M. Rozenberg, Universal electric-field-driven resistive transition in narrow-gap Mott insulators, *Adv. Mater.* **25**, 3222 (2013).
- [17] H. Yamakawa, T. Miyamoto, T. Morimoto, T. Terashige, H. Yada, N. Kida, M. Suda, H. Yamamoto, R. Kato, K. Miyagawa *et al.*, Mott transition by an impulsive dielectric breakdown, *Nat. Mater.* **16**, 1100 (2017).
- [18] P. Diener, E. Janod, B. Corraze, M. Querré, C. Adda, M. Guilloux-Viry, S. Cordier, A. Camjayi, M. Rozenberg, M. P. Besland, and L. Cario, How a dc Electric Field Drives Mott Insulators Out of Equilibrium, *Phys. Rev. Lett.* **121**, 016601 (2018).
- [19] F. Giorgianni, J. Sakai, and S. Lupi, Overcoming the thermal regime for the electric-field driven Mott transition in vanadium sesquioxide, *Nat. Commun.* **10**, 1159 (2019).
- [20] Y. Kalcheim, A. Camjayi, J. del Valle, P. Salev, M. Rozenberg, and I. K. Schuller, Non-thermal resistive switching in Mott insulator nanowires, *Nat. Commun.* **11**, 2985 (2020).
- [21] J. Zhang, A. S. McLeod, Q. Han, X. Chen, H. A. Bechtel, Z. Yao, S. N. Gilbert Corder, T. Ciavatti, T. H. Tao, M. Aronson *et al.*, Nano-Resolved Current-Induced Insulator-Metal Transition in the Mott Insulator Ca_2RuO_4 , *Phys. Rev. X* **9**, 011032 (2019).
- [22] F. Woynarovich, Excitations with complex wavenumbers in a Hubbard chain. I. States with one pair of complex wavenumbers, *J. Phys. C: Solid State Phys.* **15**, 85 (1982).
- [23] F. Woynarovich, Excitations with complex wavenumbers in a Hubbard chain. II. States with several pairs of complex wavenumbers, *J. Phys. C: Solid State Phys.* **15**, 97 (1982).
- [24] T. Oka, R. Arita, and H. Aoki, Breakdown of a Mott Insulator: A Nonadiabatic Tunneling Mechanism, *Phys. Rev. Lett.* **91**, 066406 (2003).
- [25] T. Oka and H. Aoki, Ground-State Decay Rate for the Zener Breakdown in Band and Mott Insulators, *Phys. Rev. Lett.* **95**, 137601 (2005).
- [26] M. Eckstein, T. Oka, and P. Werner, Dielectric Breakdown of Mott Insulators in Dynamical Mean-Field Theory, *Phys. Rev. Lett.* **105**, 146404 (2010).
- [27] T. Oka, Nonlinear doublon production in a Mott insulator: Landau-Dykhne method applied to an integrable model, *Phys. Rev. B* **86**, 075148 (2012).
- [28] P. Werner, K. Held, and M. Eckstein, Role of impact ionization in the thermalization of photoexcited Mott insulators, *Phys. Rev. B* **90**, 235102 (2014).
- [29] P. Stoliar, M. Rozenberg, E. Janod, B. Corraze, J. Tranchant, and L. Cario, Nonthermal and purely electronic resistive switching in a Mott memory, *Phys. Rev. B* **90**, 045146 (2014).
- [30] J. Li, C. Aron, G. Kotliar, and J. E. Han, Electric-Field-Driven Resistive Switching in the Dissipative Hubbard Model, *Phys. Rev. Lett.* **114**, 226403 (2015).
- [31] G. Mazza, A. Amaricci, M. Capone, and M. Fabrizio, Field-Driven Mott Gap Collapse and Resistive Switch in Correlated Insulators, *Phys. Rev. Lett.* **117**, 176401 (2016).
- [32] J. Li, C. Aron, G. Kotliar, and J. E. Han, Microscopic theory of resistive switching in ordered insulators: electronic versus thermal mechanisms, *Nano Lett.* **17**, 2994 (2017).
- [33] J. E. Han, J. Li, C. Aron, and G. Kotliar, Nonequilibrium mean-field theory of resistive phase transitions, *Phys. Rev. B* **98**, 035145 (2018).
- [34] H. Hirori, K. Shinokita, M. Shirai, S. Tani, Y. Kadoya, and K. Tanaka, Extraordinary carrier multiplication gated by a picosecond electric field pulse, *Nat. Commun.* **2**, 594 (2011).
- [35] Y. Iwasa, T. Koda, S. Koshihara, Y. Tokura, N. Iwasawa, and G. Saito, Intrinsic negative-resistance effect in mixed-stack charge-transfer crystals, *Phys. Rev. B* **39**, 10441 (1989).
- [36] F. Sawano, I. Terasaki, H. Mori, T. Mori, M. Watanabe, N. Ikeda, Y. Nogami, and Y. Noda, An organic thyristor, *Nature (London)* **437**, 522 (2005).

- [37] H. Kishida, T. Ito, A. Nakamura, S. Takaishi, and M. Yamashita, Current oscillation originating from negative differential resistance in one-dimensional halogen-bridged nickel compounds, *J. Appl. Phys.* **106**, 016106 (2009).
- [38] H. Kishida, T. Ito, A. Ito, and A. Nakamura, Room-temperature current oscillation based on negative differential resistance in a one-dimensional organic charge-transfer complex, *Appl. Phys. Express* **4**, 031601 (2011).
- [39] Z. Wang, H. Wu, G. W. Burr, C. S. Hwang, K. L. Wang, Q. Xia, and J. J. Yang, Resistive switching materials for information processing, *Nat. Rev. Mater.* **5**, 173 (2020).
- [40] L. Chua, Memristor-the missing circuit element, *IEEE Trans. Circuit Theory* **18**, 507 (1971).
- [41] L. O. Chua and S. M. Kang, Memristive devices and systems, *Proc. IEEE* **64**, 209 (1976).
- [42] L. Chua, Resistance switching memories are memristors, *Appl. Phys. A* **102**, 765 (2011).
- [43] D. B. Strukov, G. S. Snider, D. R. Stewart, and R. S. Williams, The missing memristor found, *Nature (London)* **453**, 80 (2008).
- [44] J. J. Yang, D. B. Strukov, and D. R. Stewart, Memristive devices for computing, *Nat. Nanotechnol.* **8**, 13 (2013).
- [45] M. Prezioso, F. Merrikh-Bayat, B. Hoskins, G. C. Adam, K. K. Likharev, and D. B. Strukov, Training and operation of an integrated neuromorphic network based on metal-oxide memristors, *Nature (London)* **521**, 61 (2015).
- [46] D. Ielmini and H.-S. P. Wong, In-memory computing with resistive switching devices, *Nat. Electron.* **1**, 333 (2018).
- [47] J. D. Kendall and S. Kumar, The building blocks of a brain-inspired computer, *Appl. Phys. Rev.* **7**, 011305 (2020).
- [48] J. Zhu, T. Zhang, Y. Yang, and R. Huang, A comprehensive review on emerging artificial neuromorphic devices, *Appl. Phys. Rev.* **7**, 011312 (2020).
- [49] M. D. Pickett and R. S. Williams, Sub-100 fJ and sub-nanosecond thermally driven threshold switching in niobium oxide crosspoint nanodevices, *Nanotechnology* **23**, 215202 (2012).
- [50] M. D. Pickett, G. Medeiros-Ribeiro, and R. S. Williams, A scalable neuristor built with Mott memristors, *Nat. Mater.* **12**, 114 (2013).
- [51] S. Kumar, J. P. Strachan, and R. S. Williams, Chaotic dynamics in nanoscale NbO₂ Mott memristors for analogue computing, *Nature (London)* **548**, 318 (2017).
- [52] S. Kumar, Z. Wang, N. Davila, N. Kumari, K. J. Norris, X. Huang, J. P. Strachan, D. Vine, A. D. Kilcoyne, Y. Nishi *et al.*, Physical origins of current and temperature controlled negative differential resistances in NbO₂, *Nat. Commun.* **8**, 658 (2017).
- [53] S. Kumar, R. S. Williams, and Z. Wang, Third-order nanocircuit elements for neuromorphic engineering, *Nature (London)* **585**, 518 (2020).
- [54] J. del Valle, P. Salev, Y. Kalcheim, and I. K. Schuller, A caloritronics-based Mott neuristor, *Sci. Rep.* **10**, 4292 (2020).
- [55] S. Tang, F. Tesler, F. G. Marlasca, P. Levy, V. Dobrosavljević, and M. Rozenberg, Shock Waves and Commutation Speed of Memristors, *Phys. Rev. X* **6**, 011028 (2016).
- [56] This was shown to be a valid approximation in similar scenarios and with relatively small fields of the order of kV/cm, see e. g., microscopic dynamical mean-field simulations in Ref. [28].
- [57] This approximation is valid at least in conditions in which large temperature increases are carefully avoided, see e. g., Refs. [7,8,35–38] and with fields of the order kV/cm, i. e., much smaller than MV/cm at which γ_{tun} becomes strongly field-dependent, see e. g., Ref. [12].
- [58] N. Strohmaier, D. Greif, R. Jördens, L. Tarruell, H. Moritz, T. Esslinger, R. Sensarma, D. Pekker, E. Altman, and E. Demler, Observation of Elastic Doublon Decay in the Fermi-Hubbard Model, *Phys. Rev. Lett.* **104**, 080401 (2010).
- [59] S. H. Strogatz, *Nonlinear Dynamics and Chaos* (CRC Press, Boca Raton, FL, 2018).
- [60] E. M. Izhikevich, *Dynamical Systems in Neuroscience* (MIT Press, Cambridge, 2007).
- [61] M. F. Ciappina, J. A. Pérez-Hernández, A. S. Landsman, T. Zimmermann, M. Lewenstein, L. Roso, and F. Krausz, Carrier-Wave Rabi-Flopping Signatures in High-Order Harmonic Generation for Alkali Atoms, *Phys. Rev. Lett.* **114**, 143902 (2015).
- [62] P. B. Corkum, Plasma Perspective on Strong Field Multiphoton Ionization, *Phys. Rev. Lett.* **71**, 1994 (1993).